Atmospheric
Chemistry
and Physics

Open Access

A new temperature- and humidity-dependent surface site density approach for deposition ice nucleation

I. Steinke[1], C. Hoose[1,2], O. Möhler[1], P. Connolly[3], and T. Leisner[1,4]

[1]Institute for Meteorology and Climate Research – Atmospheric Aerosol Research,
Karlsruhe Institute of Technology, Karlsruhe, Germany
[2]Institute for Meteorology and Climate Research – Troposphere Research,
Karlsruhe Institute of Technology, Karlsruhe, Germany
[3]School of Earth, Atmospheric and Environmental Sciences,
University of Manchester, Manchester, UK
[4]Institute for Environmental Physics, Ruprecht Karl University Heidelberg,
Heidelberg, Germany

Correspondence to: I. Steinke (isabelle.steinke@kit.edu)

Abstract. Deposition nucleation experiments with Arizona Test Dust (ATD) as a surrogate for mineral dusts were conducted at the AIDA cloud chamber at temperatures between 220 and 250 K. The influence of the aerosol size distribution and the cooling rate on the ice nucleation efficiencies was investigated. Ice nucleation active surface site (INAS) densities were calculated to quantify the ice nucleation efficiency as a function of temperature, humidity and the aerosol surface area concentration. Additionally, a contact angle parameterization according to classical nucleation theory was fitted to the experimental data in order to relate the ice nucleation efficiencies to contact angle distributions. From this study it can be concluded that the INAS density formulation is a very useful tool to describe the temperature- and humidity-dependent ice nucleation efficiency of ATD particles.

Deposition nucleation on ATD particles can be described by a temperature- and relative-humidity-dependent INAS density function $n_s(T, S_{ice})$ with

$$n_s(x_{therm}) = 1.88 \times 10^5 \cdot \exp(0.2659 \cdot x_{therm}) \ [\mathrm{m}^{-2}], \qquad (1)$$

where the temperature- and saturation-dependent function x_{therm} is defined as

$$x_{therm} = -(T - 273.2) + (S_{ice} - 1) \times 100, \qquad (2)$$

with the saturation ratio with respect to ice $S_{ice} > 1$ and within a temperature range between 226 and 250 K. For

lower temperatures, x_{therm} deviates from a linear behavior with temperature and relative humidity over ice.

Also, two different approaches for describing the time dependence of deposition nucleation initiated by ATD particles are proposed. Box model estimates suggest that the time-dependent contribution is only relevant for small cooling rates and low number fractions of ice-active particles.

1 Introduction

Aerosol particles interacting with clouds have a significant influence on the global climate by impacting cloud life cycles, precipitation formation and the global radiation budget. Interaction between clouds and aerosol particles may occur via the initiation of ice crystal formation within clouds. There are four heterogeneous ice nucleation modes involving insoluble aerosol particles (Vali, 1985). Immersion freezing occurs if a particle is already immersed within a cloud droplet when ice nucleation is initiated, whereas condensation nucleation happens shortly after or at the time of water condensation on the particle which acts as condensation and freezing nucleus at the same time. For deposition nucleation, water vapor is directly transformed into ice at the particle's surface. Contact freezing may occur if a particle collides with a supercooled droplet.

Laboratory studies and field campaigns have investigated the role of mineral dusts and single mineral species as ice nuclei in the atmosphere. Mineral dust acts as an ice nucleus over a wide range of temperatures and supersaturations over ice, with the most active dusts nucleating ice at approximately 260 K (Welti et al., 2009; Eastwood et al., 2009; Hoose and Möhler, 2012; Murray et al., 2012; Yakobi-Hancock et al., 2013). Using numerical modeling to estimate the climate impact of mineral dust through ice formation requires relations which connect aerosol properties, thermodynamic variables and resulting ice crystal concentrations. Two different approaches are typically used to find approximations to describe the measured ice formation rates, namely a nucleation rate approach based on classical nucleation theory (also called "stochastic" or "time-dependent" approach), or an ice-active surface site approach assuming a deterministic, time-independent behavior of ice nucleation ("singular hypothesis"). Both approaches are described briefly in the following paragraphs.

The deterministic approach implies that for heterogeneous ice nucleation the stochasticity is masked by the influence of variable aerosol properties (Vali, 2008). The observed ice formation seems to occur instantaneously upon cooling and does not explicitly depend on time. Therefore, the deterministic approach describes ice formation as a function of temperature and – for deposition nucleation – relative humidity over ice. The proposition of active sites which seemingly nucleate ice as soon as certain thermodynamic thresholds are reached motivates the ice nucleation active surface site (INAS) density concept (Fletcher, 1969; Connolly et al., 2009; Niemand et al., 2012; Hoose and Möhler, 2012).

The INAS density concept was applied to results from cloud chamber experiments by Connolly et al. (2009) to derive INAS densities n_s for various mineral dusts. The ice nucleation active surface site density for immersion freezing is described by

$$\Delta N = N_s \cdot (1 - \exp(-A \cdot n_s(T))),\qquad(3)$$

where ΔN is the observed ice crystal concentration at a certain temperature, N_s the initial number of droplets, A the aerosol surface and T the temperature. Note that, for immersion freezing, A exclusively refers to particles being immersed within droplets. Also, this relation (Eq. 3) is only valid for a certain aerosol particle size. Equation 3 has been expanded towards a formulation which can be applied to a polydisperse aerosol population, yielding an approximate form of the ice nucleation active surface site density valid for ice fractions smaller than $f_{ice} \approx 10\%$ (Niemand et al., 2012) with

$$n_s \approx \frac{n_{ice}}{A_{aer}},\qquad(4)$$

where n_{ice} is the observed ice crystal concentration and A_{aer} the aerosol surface area concentration.

Like the INAS density approach, classical nucleation theory formulations have already been employed in several studies investigating heterogeneous ice nucleation, e.g., in the studies by Marcolli et al. (2007). Lüönd et al. (2010), Murray et al. (2011), Wheeler and Bertram (2012), Broadley et al. (2012) and Rigg et al. (2013). Classical nucleation theory is based on the premise that the ice nucleation efficiency of aerosol particles can be quantified by the contact angle θ, which is a measure of the reduction of the energy barrier that impedes the formation of ice germs at the surface of aerosol particles (Pruppacher and Klett, 1997). For deposition nucleation, the nucleation rate $J(\theta)$ per particle is given by

$$
\begin{aligned}
J(\theta) =& 4\pi r_N^2 \cdot 4\pi r_g^2 \frac{e}{\sqrt{2\pi m_w kT}} n_1 \\
& \cdot \exp\left(-\frac{\Delta g_g(\theta)}{kT}\right) \frac{1}{n_g} \sqrt{\frac{\Delta g_g(\theta)}{3\pi kT}}
\end{aligned}
\qquad(5)
$$

following the notation used by Chen et al. (2008), with r_N being the aerosol particle radius, r_g the radius of the ice germ, e the water vapor pressure, m_w the mass of a water molecule, k the Boltzmann constant, T the temperature in [K], n_1 the number concentration of single molecules in contact with the aerosol surface, n_g the number of water molecules per ice germ and $\Delta g_g(\theta)$ the energy needed for forming a critical ice germ. Note that, to calculate n_1, the desorption energy Δg_d is set to an average value of $\Delta g_d = 4 \times 10^{-20}$ J (Chen et al., 2008). The formalism used by Chen et al. (2008) explicitly considers the temperature- and humidity-dependence of n_1 and r_g with

$$n_1 = \frac{e}{v_s\sqrt{2\pi m_w kT}} \exp\left(-\frac{\Delta g_d}{kT}\right)\qquad(6)$$

and

$$r_g = \frac{2 v_w \sigma_{i/v}}{kT \cdot \ln S_i}.\qquad(7)$$

The surface tension $\sigma_{i/v}$ is described as a temperature-dependent function according to Pruppacher and Klett (1997). The activation energy $\Delta g_g(\theta)$ is given by

$$\Delta g_g(\theta) = \frac{4\pi}{3} r_g^2 \cdot \sigma_{i/v} \cdot f(\theta),\qquad(8)$$

where $\sigma_{i/v}$ is the surface tension at the ice–vapor interface and $f(\theta) = 0.25 \cdot (2 + \cos(\theta))(1 - \cos(\theta))^2$ is the so-called form factor, with θ formally being the contact angle between particle surface and the ice germ. Physically, the form factor $f(\theta)$, which reduces the activation energy, can be taken as a measure of the ice nucleation efficiency. Several studies have pointed out that often a single contact angle is not sufficient to characterize the ice nucleation behavior of a non-homogeneous aerosol population (Marcolli et al., 2007; Lüönd et al., 2010; Wheeler and Bertram, 2012; Broadley et al., 2012; Rigg et al., 2013). Thus, the nucleation

rate approach was extended towards including not only a single contact angle but a distribution of contact angles (Marcolli et al., 2007; Lüönd et al., 2010). For this study, the distribution $p(\theta)$ is assumed to be lognormal:

$$p(\theta) = \frac{1}{\theta \sigma_\theta \sqrt{2\pi}} \exp\left(-\frac{(\ln(\theta) - \ln(\mu_\theta))^2}{2\sigma_\theta^2}\right), \qquad (9)$$

with μ_θ being the median contact angle and σ_θ the logarithmic width of the contact angle distribution.

Note that some parameterizations have sought to reconcile classical nucleation theory and the INAS density concept because both approaches offer frameworks for fitting and parameterizing experimental data, although they treat the inherent time dependence of ice nucleation differently (Vali, 1994; Niedermeier et al., 2011). However, in this study only the INAS density approach and classical nucleation theory will be compared to each other.

Besides the INAS density approach and classical nucleation theory which can be used to describe the ice nucleation efficiencies of certain well-defined aerosol species, there are also parameterizations which have been derived for either unidentified aerosols or certain subgroups of the aerosol population. Meyers et al. (1992) used laboratory data from diffusion chamber experiments to derive a saturation-dependent relation for immersion freezing and deposition nucleation. The ice crystal concentration c_{IN} [L^{-1}] is described by

$$c_{IN} = \exp[-0.639 + 0.1296 \cdot (100\,(S_{ice} - 1))], \qquad (10)$$

which is valid for temperatures between 253 and 266 K and only depends on the supersaturation over ice $S_{ice} - 1$. The parameterization developed by Phillips et al. (2008, 2012) links aerosol properties and ice crystal concentration in a more direct way by explicitly including the aerosol surface area and aerosol-specific freezing thresholds. The contribution of mineral dusts and metallic compounds to atmospheric ice nuclei ($c_{IN,DM}$) is given by

$$c_{IN,DM} = \int_{\log[0.1\,\mu m]}^{\infty} \{1 - \exp[-\mu_{DM}(D_{DM}, S_{ice}, T)]\}$$
$$\cdot \frac{dn_{DM}}{d(\log D_{DM})} d(\log D_{DM}), \qquad (11)$$

where $\mu_{DM}(D_{DM}, S_{ice}, T)$ is the average number of activated ice embryos per aerosol particle. $\mu_{DM}(D_{DM}, S_i, T)$ is defined in Phillips et al. (2008) as a function of aerosol diameter D_{DM}, temperature T in °C and the saturation over ice S_{ice}. n_{DM} is the number mixing ratio of aerosol particles belonging to the dust/metallic compounds group, given in per kg of air.

The approaches that are described in this section can all be used to develop ice nucleation parameterizations. For immersion freezing, several studies have investigated the performance of different approaches regarding the description of ice nucleation efficiencies (Hoose and Möhler, 2012; Murray et al., 2012). For deposition nucleation, only very few studies have compared different parameterizations, e.g., Wheeler and Bertram (2012). In this study deposition nucleation experiments conducted at the Aerosol Interaction and Dynamics in the Atmosphere cloud chamber (AIDA, Karlsruhe Institute of Technology) are presented and accompanied by a comparison of the INAS density approach with classical nucleation theory.

The manuscript is organized as follows: the instrumentation used at the AIDA cloud chamber and a typical deposition nucleation experiment are described in Sect. 2. In Sect. 3, the experimental results are presented, starting with ice-active fractions and ice nucleation active surface site densities. The impact of temperature, aerosol particle size and cooling rates on the observed deposition nucleation efficiency was investigated.

In this work, Arizona Test Dust (ATD, Powder Technology Inc.) is used as a substitute for naturally occurring desert dusts. ATD consists of desert dust that was washed, dried and milled in order to provide enough material in all size classes. Thus, the composition of individual ATD particles is probably more homogeneous than the composition of original desert dusts, and also the surface properties may differ from natural dusts.

Several sets of experimental runs were conducted, starting at approximately 250, 235 or 223 K. In order to investigate the impact of time dependence and variations in the aerosol size distribution on the deposition nucleation efficiency of ATD, the experimental cooling rate was varied between 0.3 and 2.9 K min^{-1}, and also the aerosol size distribution was varied by either including or discarding particles larger than about 1 µm.

In Sect. 3, ice nucleation thresholds, INAS densities and contact angle distribution parameters as derived from the experimental data are presented. Additionally, an average INAS density function is derived and compared to two empirical parameterizations (Meyers et al., 1992; Phillips et al., 2008) with regard to their sensitivity to temperature and relative humidity over ice.

In the last part of Sect. 3, the relevance of time dependence for deposition nucleation initiated by ATD particles is investigated by using either a linear time-dependent source term or a time-dependent exponential function in addition to the formerly time-independent average INAS density relation. The average INAS density function, both with and without the time-dependent contributions, was then tested with the box model ACPIM (Aerosol–Cloud Precipitation Interaction Model) regarding the impact of variations in cooling rate and aerosol number concentration on the observed ice fractions. The modeling results are presented at the end of Sect. 3.
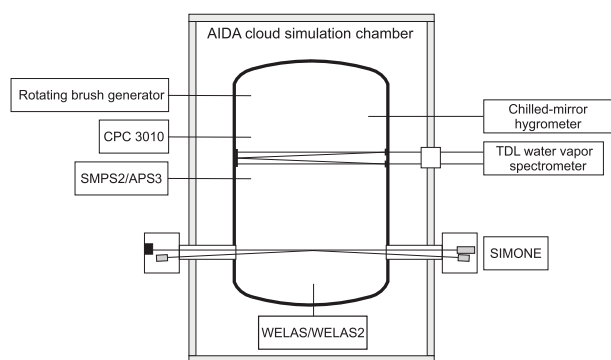
Figure 1. Schematic drawing of the AIDA cloud chamber: aerosol instrumentation (rotating brush generator, APS, SMPS, CPC3010), instruments used for characterization of the droplet/ice crystal population (welas/welas2, SIMONE) and humidity measurements (TDL, chilled-mirror hygrometer).

2 Experimental methods

The experiments presented in this study were conducted at the AIDA cloud chamber facility, located at the Karlsruhe Institute of Technology. With the AIDA cloud chamber, the ascent of air parcels can be simulated by expanding moist air within the chamber vessel. Thus, the ice nucleation properties of various aerosol types can be investigated under atmospherically relevant conditions for mixed-phase and cirrus clouds.

Figure 1 shows a schematic drawing of the AIDA cloud simulation chamber: the cloud chamber itself is enclosed by a thermally isolated housing. With two pumps the chamber volume can be expanded at controllable rates corresponding to defined cooling rates. Background aerosol concentrations within the cloud chamber were typically below $0.1\,\mathrm{cm^{-3}}$.

On the left side of Fig. 1, the aerosol instrumentation is shown. A rotating brush generator (RBG 1000, Palas) is used for dry dispersion of the dust samples. Additionally, cyclone impactors are generally used to eliminate particles larger than about $1\,\mu\mathrm{m}$. Aerosol number concentrations are measured with a condensation particle counter (CPC3010, TSI), whereas the aerosol size distribution was measured by combining SMPS (Scanning Mobility Particle Sizer – TSI) and APS (Aerodynamical Particle Sizer – TSI) measurements. From these data, the total aerosol surface area concentration can be inferred by translating the size distribution into a surface distribution after converting mobility and aerodynamic diameters into equivalent sphere diameters (Möhler et al., 2008). To this surface distribution a lognormal fit is applied from which the total aerosol surface area concentration can be estimated through integrating the distribution. An exemplary aerosol surface distribution is shown in Fig. 2. Note that APS and SMPS data in combination cover the whole size range.
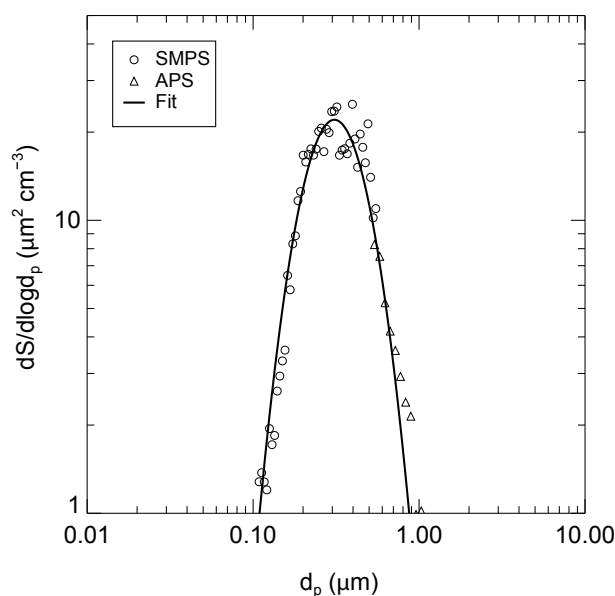

Figure 2. Aerosol surface distribution for dust particles (Arizona Test Dust) with lognormal fit: $d_{\mathrm{med,\,surf}} = 0.32\,\mu\mathrm{m}$; $\sigma_{\mathrm{surf}} = 1.55$ (exp. IN17_04).

Values for the relative humidity over ice (RH_{ice}) and over water (RH_{water}) are derived from tunable diode laser (TDL) absorption spectroscopy measurements. Infrared absorption is measured at a wavelength around $\lambda = 1.37\,\mu\mathrm{m}$ and converted into water vapor concentrations with an accuracy of $\pm 5\,\%$ (Fahey et al., 2014). From these water vapor concentration values, the relative humidities RH_{water} and RH_{ice} are calculated using the water vapor saturation pressures over liquid water and ice (Murphy and Koop, 2005) and measurements of the gas temperature in the cloud chamber. The total water content is also measured by a chilled-mirror hygrometer. For the deposition nucleation experiments, however, only the TDL measurements were considered.

The AIDA cloud chamber is also equipped with several optical instruments (Wagner et al., 2009) – three of these instruments (welas, welas2 and SIMONE (Scattering Intensity Measurements for the Optical Detection of Ice)) are also sketched in Fig. 1. Ice crystal concentrations are derived from the particle concentrations and size distributions measured with two optical particle counters (welas and welas2, Palas GmbH). Particle sizes are calculated from the intensity of light scattered by particles crossing the beam of an internal white light source. Note that aerosol particles, droplets and ice crystals are detected alike if they are large enough to scatter sufficient light into the detector, but only ice crystals grow rapidly to sizes which eventually exceed those of the initial aerosol particles. Droplet formation is expected to be negligible during the experimental runs presented in this work because ice nucleation was only investigated in conditions subsaturated with respect to liquid water, and the
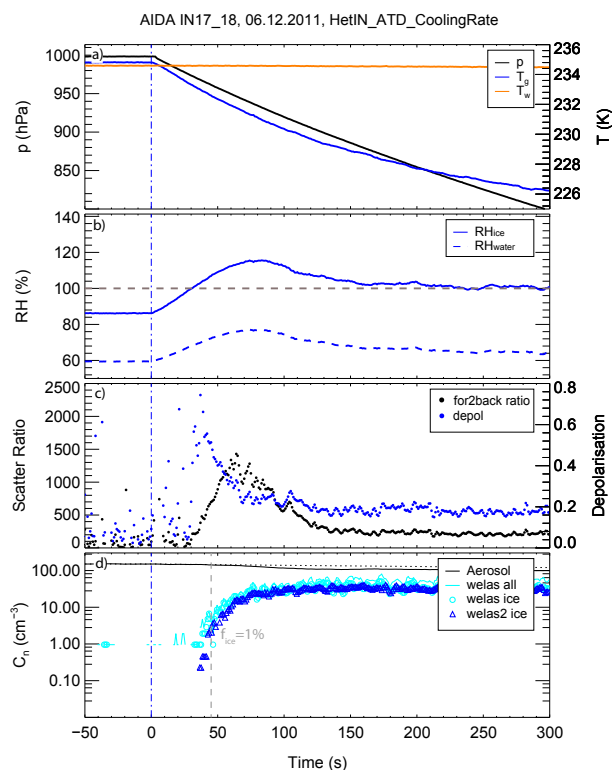
Figure 3. Time series for an AIDA expansion experiment investigating deposition nucleation initiated by Arizona Test Dust. **(a)** Variation of thermodynamical variables during expansion: decrease in gas temperature T_g and pressure p; temperature at the walls of the vessel (T_w) stays approximately constant. **(b)** Relative humidity over water and over ice as derived from TDL data. **(c)** Forward-to-backward scattering ratio and depolarization of the backward-scattered light as measured by SIMONE. **(d)** Aerosol number concentration (CPC3010) and ice crystal concentrations (welas/welas2).

amount of soluble components is expected to be very small (Vlasenko et al., 2005). The distinction between aerosol particles and ice crystals is made by selecting a suitable size threshold. The formation of small ice crystals is also indicated by the change in depolarization detected by SIMONE (Schnaiter et al., 2012). SIMONE is used for observing scattering signals from particles crossing the pathway of a polarized laser beam ($\lambda = 488$ nm) which horizontally traverses the cloud chamber. Besides scattering in forward (at 2°) and near-backward (at 178°) direction, the depolarization is measured using a Glan laser prism to separate the parallel and the perpendicular polarized components of the near-backward-scattered light.

The course of a typical AIDA expansion experiment is depicted in Fig. 3 and briefly described in the following paragraphs. The first panel shows the pressure p, which decreases during an expansion run; the gas temperature T_g within the vessel drops simultaneously. During this expansion experiment, the pressure p within the AIDA vessel is lowered

from ambient pressure to approximately 800 mbar. The starting temperature was 235 K, whereas the minimum temperature was about 226 K. Over the course of an expansion experiment, the temperature T_w at the chamber walls remains virtually unchanged. Panel b depicts the relative humidity values (RH$_{water}$ and RH$_{ice}$) as derived from the TDL measurements. Water saturation is not reached during this experiment. Therefore, neither significant droplet activation nor immersion freezing can occur: ice crystals form almost completely by deposition nucleation. The peak relative humidity over ice was about 118 %.

Figure 3c shows the forward-to-backward scattering ratio as derived from the SIMONE scattering signals alongside the depolarization signal measured for the backward-scattered light. The ice nucleation onset with the formation of small ice crystals is indicated by an increase in depolarization as well as a slightly delayed increase of the forward-to-backward scattering ratio. The increase in depolarization is a further indication that only deposition nucleation was observed because the formation of spherical droplets leads to a clear decrease in the depolarization signal. The last panel in Fig. 3 shows the aerosol concentration (measured by CPC3010) and the ice crystal concentrations (derived from welas/welas2 data). The aerosol concentration given per cubic centimeter decreases over the course of the experiment due to the volume expansion. The ice crystal concentration as derived from the welas/welas2 data shows a steep onset at approximately RH$_{ice}$ = 103 %. The maximum fraction of ice-active particles observed during this experiment was f_{ice} = 40 %. Note that for the calculation of the ice nucleation active surface site densities only ice fractions $f_{ice} < 10$ % were considered. Initially, the growing ice particles deplete the vapor phase only negligibly, and relative humidity over ice is an almost linear function of temperature.

Table 1 lists all experimental runs that were conducted as a part of this study. All AIDA expansion experiments described in Table 1 started at 250, 235 or 223 K. The cooling rate was varied between 0.3 and 2.9 K min^{-1} as indicated. Note that the cooling rate determines the timescale that is relevant to the observed ice nucleation processes and thus gives experimental access to the time dependence of heterogeneous ice nucleation. Additionally, the aerosol surface area concentration was varied either by changing the aerosol number concentration or by including particles larger than ca. 1 µm.

For the experiments starting at 250 K, the cooling rate was varied between 0.3 and 2.7 K min^{-1}. The variations of the aerosol surface area concentration during these experiments were achieved by varying the aerosol number concentration. In addition to varying the cooling rate between 0.7 and 2.9 K min^{-1} and to systematically changing the aerosol number concentration, two experiments starting at about 235 K (exps. 14 and 15) were conducted without using cyclone impactor stages, which resulted in a shift of the aerosol size distribution towards larger particles. The ice nucleation effi-

Table 1. Overview of ice nucleation experiments with ATD as carried out at the AIDA cloud chamber; reference experiments (without ATD particles) being omitted – experiments not employing cyclone impactor stages are marked by an asterisk; experiments are grouped according to the temperatures at the beginning of each individual run.

Experiment number	T_{start} [K]	Humidity threshold [%]	Aerosol concentration [cm^{-3}]	Median diameter [μm]	Aerosol surface area concentration [μm^2 cm^{-3}]	Cooling rate [K min^{-1}]	Experiment name
1	250.2	120.6	99	0.25	23	0.3	IN17_01
2	249.2	119.8	137	0.24	40	0.6	IN17_02
3	249.9	119.6	43	0.24	9	0.5	IN17_04
4	249.7	119.5	38	0.21	10	0.3	IN17_06
5	250.1	120.8	62	0.24	17	0.3	IN17_08
6	249.8	119.3	44	0.24	14	2.5	IN17_10
7	249.8	121.1	504	0.23	120	2.7	IN17_11
8	249.7	–	508	0.23	126	0.8	IN17_12
9	250.2	–	500	0.24	139	0.4	IN17_13
10	234.7	104.3	22	0.22	6	1.0	IN17_15
11	235.3	108.4	26	0.20	9	2.9	IN17_16
12	234.8	105.4	151	0.23	39	2.8	IN17_18
13	234.8	103.4	107	0.19	18	1.1	IN17_21
14	235.5	100.4	171	0.37	162	1.1	IN17_22*
15	235.0	101.1	139	0.35	209	1.1	IN17_24*
16	235.4	103.4	48	0.22	13	0.7	IN17_26
17	222.8	104.4	451	0.22	100	2.4	IN15_04
18	222.7	102.2	809	0.24	201	2.7	IN15_12

ciency was also investigated at colder temperatures, i.e., for expansion runs starting at approximately 223 K.

3 Experimental results

The deposition nucleation experiments described in Table 1 are used to derive different measures for the ice nucleation efficiencies. In particular, humidity thresholds at ice nucleation onset, INAS densities and contact angle distribution parameters were analyzed.

3.1 Ice nucleation properties of ATD

3.1.1 Thermodynamic ice nucleation thresholds

Figure 4 shows trajectories in the T/RH_{ice} space for all AIDA expansion experiments listed in Table 1. Also, the temperature and humidity conditions at which an ice fraction $f_{ice} = 1\%$ was observed are represented. All trajectories in Fig. 4 start shortly after ice formation was observed and end when ice crystal growth leads to a deviation from the initially linear increase in RH_{ice}. Note that all experimental runs began at initially subsaturated conditions with respect to ice. For the experiments starting at about 250 K, ice nucleation occurs for relative humidity values between 112 and 125 %, whereas for temperatures below 235 K ice nucleation is already observed slightly above saturation with respect to ice. From Fig. 4 it can also be observed that trajectories for ex-
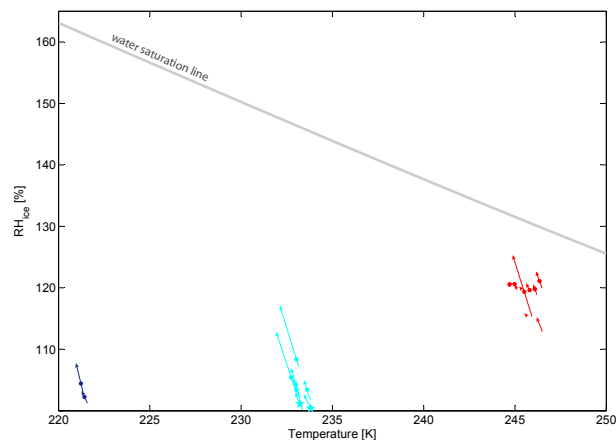

Figure 4. Trajectories of ice nucleation experiments with ice nucleation thresholds: trajectories are shown from the point when ice crystal concentrations first exceed background concentrations, with only the part being shown for which RH_{ice} increases almost linearly with decreasing temperature; relative humidity over ice corresponding to an ice-active particle fraction $f_{ice} = 1\%$ is indicated by ● for standard experiments using cyclone impactors to define an aerosol size cutoff, and ★ for experiments including larger particles.

periments starting below 235 K are more similar to each other than those of the experiments at warmer temperatures.

The relative humidity values (RH_{ice}), for which an ice number fraction $f_{ice} = 1\%$ was observed, are considered as
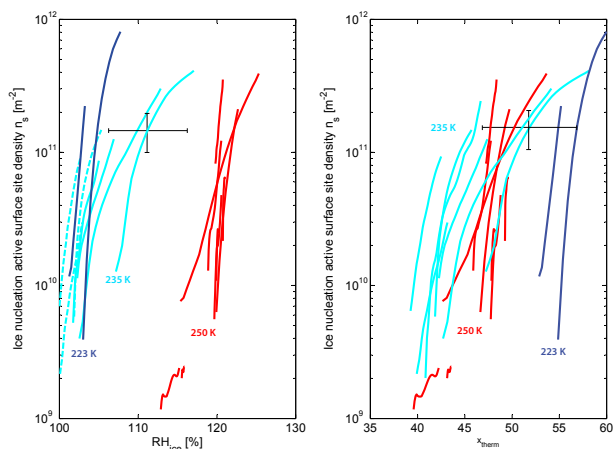
Figure 5. Ice nucleation active surface site densities n_s for all experiments starting at 223, 235 or 250 K: INAS densities are depicted with respect to relative humidity over ice (left) and with respect to the temperature- and saturation-dependent function $x_{therm}(T, S_{ice})$ (right) with $x_{therm}(T, S_{ice}) = -(T - 273.2) + (S_{ice} - 1) \times 100$; dashed lines represent experiments including larger particles. The error bars represent the measurement uncertainties with $\Delta n_s / n_s \approx 35\%$ and $\Delta x_{therm} \approx 5$.

Figure 6. Ice nucleation active surface site densities as in Fig. 5 with exponential fit function (excluding the experiments starting at $T_{start} = 223$ K); the grey dashed lines indicate deviations from the fitting function by an order of magnitude.

ice nucleation thresholds in this study. These ice nucleation thresholds are depicted in Fig. 4 for all experiments. For the experiments starting at 250 K, the ice nucleation thresholds scatter around $RH_{ice} \approx 120\%$. Note that for two experiments the ice fraction remained below $f_{ice} = 1\%$. The humidity threshold values suggest that warm-temperature deposition nucleation does not depend primarily on the cooling rate. At lower temperatures ($T_{start} \approx 235$ K and $T_{start} \approx 223$ K), the ice nucleation thresholds mostly scatter around $RH_{ice} \approx 104\%$. Only the two experiments which investigated the influence of larger particles (exps. 14 and 15) are characterized by ice nucleation starting already slightly above saturation with respect to ice. This finding agrees with other studies finding that larger particles lower the observed ice nucleation thresholds (e.g., Welti et al., 2009).

It should be noted that the spread of the observed humidity threshold values – considering experiments with a similar starting temperature – lies within the measurement uncertainty $\Delta RH_{ice} = \pm (3–5)\%$. Only for experiments including larger particles a shift towards lower ice nucleation thresholds is observed. Therefore, deposition nucleation seems to be only weakly time dependent over the range of variations in cooling rate and aerosol surface area concentrations investigated in this study. If ice nucleation had to be described by a time-dependent heterogeneous nucleation rate approach, the freezing thresholds would have been shifted towards lower relative humidities for low cooling rates. Because neither a completely singular behavior (i.e., always the same ice nucleation threshold) nor a relation between cooling rate and thresholds could be deduced from our measurements, it is
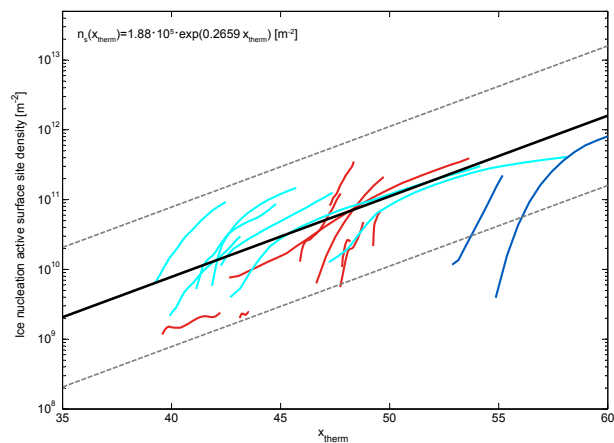
not possible to directly infer the influence of different cooling rates (corresponding to ice nucleation timescales) on the observed ice fraction. Therefore, the impact of time dependence will be investigated in more detail in the following subsections.

Figure 4 also shows that the ice nucleation thresholds are clearly divided into two groups depending on the ambient temperature, with higher humidity thresholds at $T_{start} \approx 250$ K and lower ice nucleation thresholds for the experiments at colder temperatures ($T_{start} \approx 235$ K and $T_{start} \approx 223$ K). Therefore, it can be also concluded that the deposition nucleation efficiency of ATD particles depends not only on relative humidity, but also on temperature.

3.1.2 Ice nucleation active surface site densities

The ice nucleation efficiency can also be expressed as the INAS density averaged over the whole aerosol population for each experiment. The INAS density values (Niemand et al., 2012) are calculated from

$$n_s = n_{ice} / A_{aer} \ [\text{m}^{-2}] \tag{12}$$

with the ice crystal concentration n_{ice} [cm^{-3}] and the total aerosol surface area concentration A_{aer} [µm^2 cm^{-3}]. Note that n_s can also be interpreted as a way of normalizing ice crystal concentrations.

The INAS densities are depicted in Fig. 5 with respect to RH_{ice} (left) or with respect to a function x_{therm} (right) which is defined as

$$x_{therm} = -(T - 273.2) + (S_{ice} - 1) \times 100 \tag{13}$$

Note that in Eq. (13), T represents the numerical value of the average temperature within the cloud chamber in [K] and is therefore dimensionless. S_{ice} corresponds to the ice saturation ratio. Equation (13) can be understood as a very generic
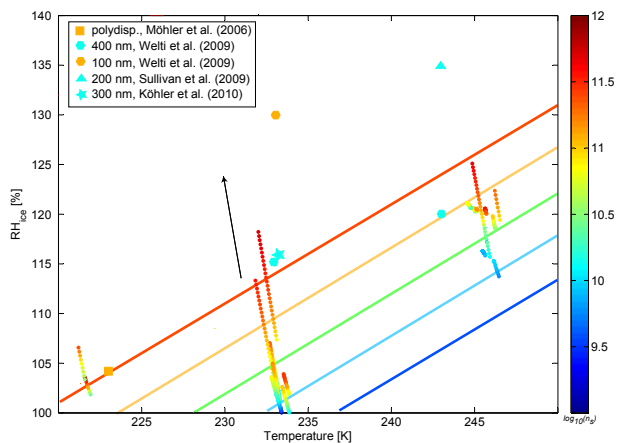
Figure 7. n_s trajectories derived from experimental runs (see Table 1) – the arrow indicates decreasing temperature and increasing RH_{ice} during expansion experiments (see Fig. 4); colored lines correspond to isolines of the fitted INAS density ($\log_{10}(n_s)$) from Fig. 6 – symbols indicate ice nucleation active surface site densities derived from experimental studies by other authors (same color code as for isolines).

Figure 8. Comparison between ice nucleation active surface site densities derived from this work (colored lines), the dust-adapted parameterization by Phillips et al. (2012) (colored dashed lines) and the parameterization by Meyers et al. (1992) (black dashed line); for the Phillips parameterization, colors indicate the same temperatures as for our parameterization, whereas the Meyers parameterization is not temperature dependent ($A_{aer} = 2 \times 10^{-6} \mathrm{m^2\,m^{-3}}$) – the grey dashed line indicates the upper limit for n_s values derived from expansion experiments presented in this study.

and simple way to describe the combined dependence of deposition nucleation on temperature and relative humidity over ice within a certain range of thermodynamic conditions. More general formulations of Eq. (13) would read

$$x_{therm} = -\alpha(T) \cdot (T - 273.2) + (1 - \alpha(T)) \cdot (S_{ice} - 1) \times 100 \quad (14)$$

or

$$x_{therm} = -\alpha(T) \cdot (T - 273.2) + \beta(T) \cdot (S_{ice} - 1) \times 100, \quad (15)$$

with $\alpha(T)$ and $\beta(T)$ being temperature-dependent weighting coefficients. However, the improvement of fits relying on Eqs. (14) or (15) was only marginal for the temperature and humidity conditions investigated in this study. Note also that x_{therm} as a linear function in humidity and temperature is assumed to be only strictly valid between 226 and 250 K. Other studies show that the n_s isolines for deposition nucleation caused by materials such as hematite are strongly temperature dependent between 223 and 237 K, but not between 223 and 213 K (Hiranuma et al., 2014). Thus, these results suggest that different x_{therm} or other approaches might be needed within different temperature regimes. Also, deposition nucleation close to water saturation may coincide with pore condensation freezing (Marcolli et al., 2014).

In Fig. 5 (left) the two groups of experiments starting at 235, 223 or 250 K are clearly separated. Thus, in agreement with the behavior of the ice nucleation thresholds, Fig. 5 (left) confirms that, within the temperature range between 223 and 250 K, deposition nucleation as a process does not only depend on RH_{ice} but is also strongly controlled by temperature. Also, experiments including larger particles (dashed lines in Fig. 5) are characterized by similar INAS densities to the experiments targeting a narrow
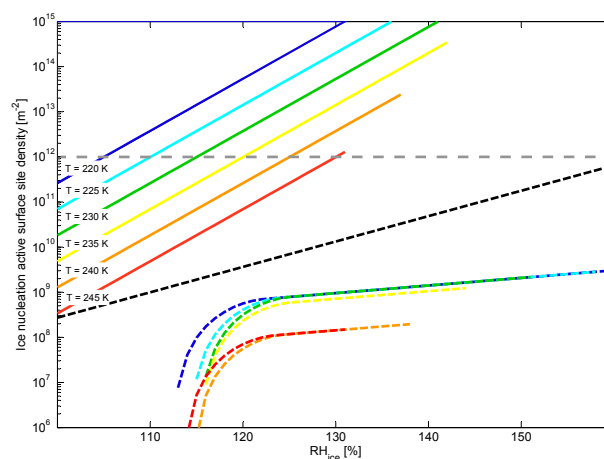
particle size distribution. Therefore, within this experimental setup, aerosol particle size does not impact the observed INAS density values much. This finding supports the concept of a surface-area-related density of ice nucleation sites.

By representing the INAS densities as a function of relative humidity and temperature (Fig. 5, right), the INAS trajectories representing warm-temperature deposition nucleation fall much closer together, which means that deposition nucleation can be described by the change in x_{therm} as defined by Eq. (13). Note that the length of each n_s trajectory generally corresponds to a time period of $\Delta t \leq 25\,s$ starting at the first observation of ice nucleation. For experiments during which the growth of ice crystals led to an early deviation from the linear increase of relative humidity over ice, this time interval Δt was chosen to be shorter than 25 s in order to minimize systematic errors of the measured ice crystal concentrations caused by the settling of ice crystals. The time interval Δt was defined with regard to excluding reductions of the observed ice crystal concentration by sedimentation, assuming that the largest ice crystals grow to approximately 100 μm. These large crystals determine the sedimentation timescale and sediment with terminal velocities between 0.1 and $10\,\mathrm{cm\,s^{-1}}$ (Westbrook, 2008). This corresponds to sedimentation times between 35 and 3500 s for an average fall distance of 3.5 m (half of the cloud chamber height). Thus, as a conservative estimate the timescale was chosen to be $\Delta t = 25\,s$ since the maximum dimensions of the observed ice crystals were not measured directly.

The n_s trajectories as shown in Fig. 5 are afflicted with two sources of uncertainty, of which the n_s values themselves are the first source. The measurement uncertainty of n_s is determined by the uncertainties of n_{ice} and A_{aer}, with $\Delta n_{ice}/n_{ice} \approx 25\%$ and $\Delta A_{aer}/A_{aer} \approx 25\%$, which results in $\Delta n_s/n_s \approx 35\%$. Secondly, the position of each trajectory within the T/RH_{ice} space is affected by the uncertainties $\Delta T = \pm 0.3\,K$ and ΔRH_{ice} up to 5%. These uncertainties then translate into an uncertainty of the thermodynamic variable x_{therm}, with $\Delta x_{therm} \approx 5$. Figure 5 shows that the experiments at higher relative humidities over ice (corresponding to warmer starting temperatures at about 250 K) are characterized by a much larger variation in the slopes of INAS density trajectories than the experiments at lower relative humidities over ice (corresponding to colder temperatures).

3.2 Ice nucleation active surface site density approach and comparison to other parameterizations

In this section, we will first present an overall INAS density fit to all measurements above 226 K. This means that the two measurements starting at 223 K will be excluded. The average INAS density function is then compared to the dust-adapted parameterization by Phillips et al. (2012) and the parameterization by Meyers et al. (1992), which does not distinguish between different aerosol species. Complementing the INAS density approach, also results from fitting nucleation rates according to classical nucleation theory to the measured ice fractions are presented. Additionally, in the last subsection, the time dependence of deposition nucleation initiated by ATD particles is expressed as either a linear source term or a time-dependent exponential function.

3.2.1 General ice nucleation active surface density approach

Figure 5 shows that the n_s values observed for temperatures above 226 K do not diverge by more than 1 order of magnitude, which suggests that the INAS density values may be described by an average n_s function. According to least-square fitting, all measurements above 226 K can be described by the fit function

$$n_s(x_{therm}) = 1.88 \times 10^5 \cdot \exp(0.2659 \cdot x_{therm})\ [m^{-2}]. \quad (16)$$

The measurements together with the fit ($r^2 = 0.49$) are depicted in Fig. 6. Note that the quality of the fit only slightly improves by defining x_{therm} as

$$x_{therm} = -1.085 \cdot (T - 273.2) + 0.815 \cdot (S_{ice} - 1) \times 100 \quad (17)$$

instead of using Eq. (13).

Figure 7 shows all measured n_s values corresponding to the T/RH_{ice} trajectories of each experimental run listed in Table 1. Isolines with constant INAS density values indicate the increase of the fit function $n_s(x_{therm})$ with supercool-

ing and relative humidity over ice. The measurement uncertainties are given by $\Delta T = \pm 0.3\,K$, ΔRH_{ice} up to 5% and $\Delta n_s/n_s \approx 35\%$.

For comparison, n_s values from other experimental studies (see references) investigating the ice nucleation properties of ATD in the deposition nucleation mode are shown. Note that the experimental setups which were used to derive the INAS densities differ among these studies. INAS densities calculated for previous AIDA cloud chamber experiments with ATD agree well with $n_s(x_{therm})$ from Eq. (16) (Möhler et al., 2006).

INAS densities were also derived from ice fractions f_{ice} observed in studies investigating the deposition nucleation mode properties of monodisperse ATD particles (Koehler et al., 2010; Sullivan et al., 2010; Welti et al., 2009) with

$$n_s = f_{ice}/(\pi d^2), \quad (18)$$

where d is the diameter of the size-selected ATD particles. The particle size selection in the aforementioned studies was achieved by using differential mobility analyzers (DMAs). Note that in Fig. 7 the nominal particle diameters of the size-selected particles are indicated. The INAS densities derived from the studies by Koehler et al. (2010); Sullivan et al. (2010) and Welti et al. (2009) generally differ by more than 1 order of magnitude from our fitted $n_s(x_{therm})$. In the study by Koehler et al. (2010) a continuous flow diffusion chamber was used to investigate the ice nucleation properties of ATD particles with selected diameters of 200, 300 or 400 nm. A continuous flow diffusion chamber was also used by Sullivan et al. (2010), who investigated monodisperse ATD particles ($d = 200$ nm). Welti et al. (2009) investigated the deposition nucleation properties of size-selected ATD particles with the Zurich Ice Nucleation Chamber (ZINC). In all studies, the ATD sample was dispersed by using either a rotating brush generator or a fluidized bed generator. The INAS density values derived from the aforementioned studies are much lower than the INAS densities derived within this experimental study. These deviations might be partially explained by differences in the temperature and humidity profiles compared to the AIDA experiments.

3.2.2 Comparison to other parameterizations

Figure 8 shows a comparison between the INAS densities from the $n_s(x_{therm})$ parameterization (Eq. 16), the ice formation as parameterized by Phillips et al. (2008, 2012) and the ice crystal concentration derived by using the purely humidity-dependent parameterization proposed by Meyers et al. (1992). For our calculations we assume that the ice was formed on a generic aerosol population with an aerosol surface area concentration of $A_{aer} = 2 \times 10^{-6}\,m^2\,m^{-3}$ as proposed in Phillips et al. (2012). The grey dashed line in Fig. 8 indicates the upper limit of observed ice nucleation active surface site densities in this study ($f_{ice} < 10\%$). The INAS density lines as shown in Fig. 8 are also restricted by deposi-
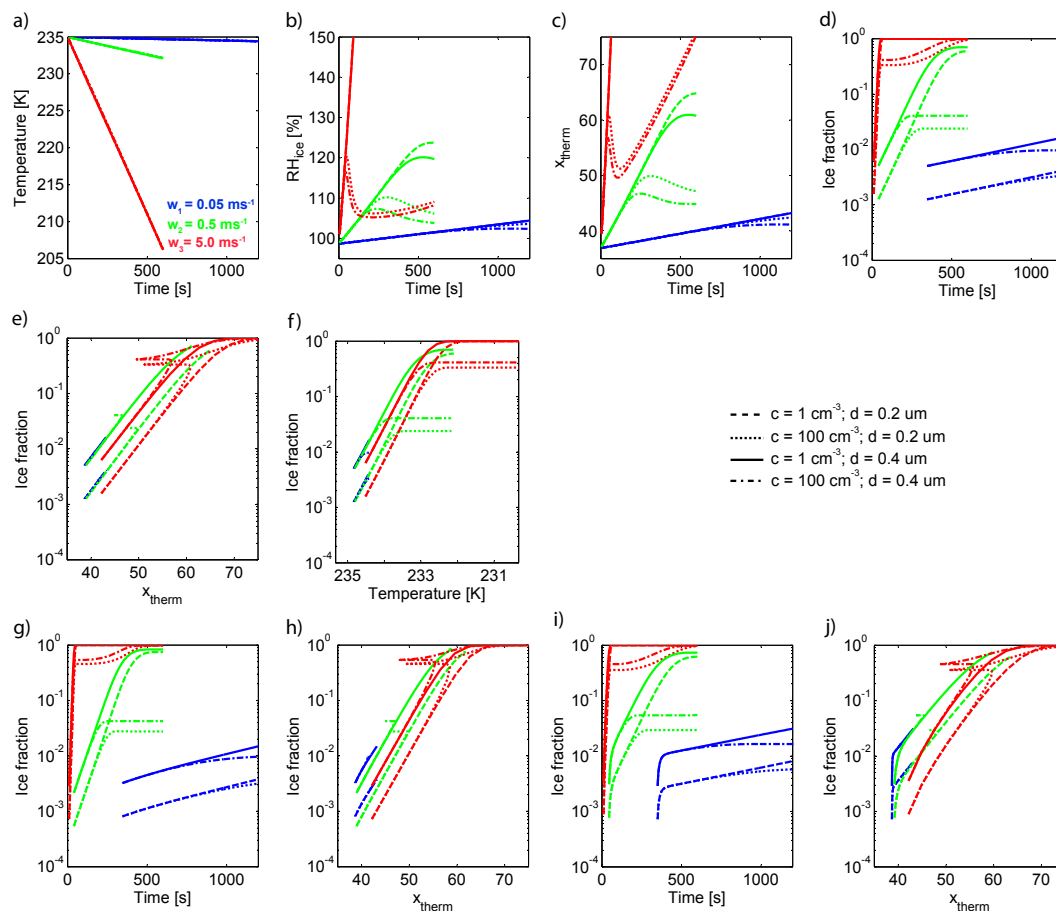
Figure 9. Time series for calculations with the box model ACPIM: parcel runs with varying updraft velocities (indicated by color as noted in panel **a**) for investigating the influence of aerosol concentration and the aerosol median diameter on the observed ice-active fractions; all runs start at $T = 235\,\mathrm{K}$ and $S_{\mathrm{wat}} = 0.68$ – the first panels (**a–c**) show temperature, relative humidity and the composite variable x_{therm}; for the subfigures (**d**), (**e**) and (**f**) ice nucleation is parameterized by Eq. (16), whereas for (**g**) and (**h**) Eq. (19) was used and for (**i**) and (**j**) Eq. (21) was used .

tion nucleation occurring only below water saturation. Note that for this comparison not the absolute INAS density values are considered to be most relevant but rather the slopes of the n_{s} curves, because the absolute values also depend on the assumed aerosol surface area concentration A_{aer}. Nevertheless, in a recent immersion freezing study ice crystal concentrations derived from an INAS density parameterization based on cloud chamber experiments with desert dusts were observed to differ by more than 1 order of magnitude from estimates made with the Phillips parameterization for immersion freezing at temperatures above 255 K (Niemand et al., 2012).

For deposition nucleation, the parameterizations by Phillips et al. (2012) and Meyers et al. (1992) predict INAS densities with significantly smaller slopes (i.e., humidity dependence) compared to the results from our ATD measurements. Additionally, the temperature dependence of the parameterization by Phillips et al. (2012) is weaker, whereas the parameterization by Meyers et al. (1992) is a priori, not

considering any changes in supercooling. Applied in climate models, parameterizations describing deposition nucleation without considering the temperature dependence will predict largely deviating ice crystal concentrations in comparison to calculations based on our parameterization.

3.2.3 Comparison to classical nucleation theory

Classical nucleation theory can be used to fit results from deposition nucleation experiments with ATD particles. For each experimental run, the observed ice nucleation efficiency can be expressed by an apparent median contact angle μ_θ and an apparent contact angle distribution width σ_θ. These parameters μ_θ and σ_θ can be derived from using Eqs. (5), (8) and (9) to fit the observed ice fractions.

For most experiments, the aerosol size distribution was assumed to be lognormal, with the median diameter $\mu_{\mathrm{d}} = 0.23\,\mu\mathrm{m}$ and the geometric size distribution width $\sigma_{\mathrm{d}} = 1.56$. Only for the experiments without cyclone impactors (i.e.,

larger particle being present) were the aerosol size distribution parameters chosen to be $\mu_d = 0.35\,\mu m$ and $\sigma_d = 1.73$.

For the experiments starting at about 250 K, the median contact angles μ_θ vary between 17 and 48° (excluding one outlier), whereas for experimental runs starting at about 235 or 223 K the median contact angles μ_θ were found to scatter between 25 and 39° and between 8 and 13°.

For deposition nucleation observed during experiments starting at higher temperatures around 250 K, the contact angle distribution parameters which best described all experimental runs ($r^2 = 0.48$) were $\mu_\theta = 22.1°$ and $\sigma_\theta = 0.095$. For deposition nucleation at lower temperatures, the contact angle parameters were found to be $\mu_\theta = 36.2°$ and $\sigma_\theta = 0.520$ ($r^2 = 0.52$) for experiments at $T_{start} \approx 235$ K, and $\mu_\theta = 16.9°$ and $\sigma_\theta = 0.540$ ($r^2 = 0.89$) at $T_{start} \approx 223$ K.

The contact angle parameters derived from the ATD experiments presented in this study vary considerably between different experimental runs and also slightly depend on the thermodynamic conditions (i.e., temperature and relative humidity over ice). The nucleation rate approach with the assumption of a lognormally distributed range of contact angles did not result in a consistent set of fit parameters for the available data set.

Note that, even though both T and S_{ice} enter the classical nucleation theory formulation of the nucleation rate J_{het}, the dependence on S_{ice} is much stronger than the dependence on T. This can be seen, e.g., in Fig. A1 of Hoose and Möhler (2012) by the near-horizontal isolines of J_{het}. The experimentally observed T and S_{ice} dependence in this study, however, is markedly different from the CNT prediction.

More experimental studies in a wider range of temperature, aerosol surface area and cooling rate may provide a better basis for constraining the results from nucleation rate fits to measured ice formation rates.

3.3 Time dependence of deposition nucleation and extension of the ice nucleation active surface site density concept

Ice nucleation active surface site densities as defined by Eq. (12) depend only on temperature and relative humidity over ice. Considering time-dependent ice formation in the $n_s(x_{therm})$ fits requires an extension of the functional form as stated in Eq. (16) by time-dependent terms. Two different approaches are used for describing the time-dependent contribution to ice formation.

Time dependent ice nucleation may be described by

$$n_s = \widetilde{n}_s + a_3 \cdot t \tag{19}$$

$$= a_1 \cdot \exp(a_2 \cdot x_{therm}) + a_3 \cdot t \quad [\mathrm{m}^{-2}], \tag{20}$$

where x_{therm} is defined by Eq. (13) and t [s] is the time starting from the first observation of ice crystals, neglecting ice formation below the detection limit. To derive the coefficients in Eq. (19), only the first 25 s after ice formation was

Table 2. Overview of updraft velocities and aerosol properties as used for the trajectories calculated with the box model ACPIM.

Aerosol concentration [cm^{-3}]	1	100	
Aerosol particle median diameter [μm]	0.2	0.4	
Updraft velocity w [m s^{-1}]	0.05	0.5	5.0

observed are considered. The first part of Eq. (19), expressed as $\widetilde{n}_s$, describes the formation of ice crystals caused by the "best" ice nuclei among the dust particles. Upon reaching certain thermodynamic thresholds (i.e., x_{therm} values) these particles initiate ice nucleation immediately within the temporal resolution of our experimental setup. The linear source term then describes the formation of ice by the less efficient ice nuclei components, which (at comparable x_{therm} conditions) have lower freezing probabilities and are only activated after a certain period of time. Therefore, this linear contribution will become apparent especially at low cooling rates. The coefficients in Eq. (19) are determined from least-square fitting as $a_1 = 1.9 \times 10^3$ [m^{-2}], $a_2 = 0.363$ and $a_3 = 3.7 \times 10^6$ [m^{-2} s^{-1}] ($r^2 = 0.74$).

A second time dependence parameterization assumes that there is a certain ice nucleation active surface site density $\widetilde{n}_s(x_{therm})$ towards which the measured INAS densities would converge eventually at a certain x_{therm} value. This time-dependent behavior is then described by

$$n_s = \widetilde{n}_s \cdot (1 - \exp(-b_3 \cdot t)) \tag{21}$$

$$= b_1 \cdot \exp(b_2 \cdot x_{therm}) \cdot (1 - \exp(-b_3 \cdot t)) \quad [\mathrm{m}^{-2}]. \tag{22}$$

Again, the coefficients are derived from the measurements for ice fractions smaller than $f_{ice} < 10\,\%$. The coefficients in Eq. (21) are determined as $b_1 = 6.1 \cdot 10^5$ [m^{-2}], $b_2 = 0.254$ and $b_3 = 0.065$ [s^{-1}] ($r^2 = 0.70$).

Note, however, that Eqs. (19) and (21) need to be viewed as very simplistic approaches. Nevertheless, these equations could be used to evaluate the time dependence of ice nucleation initiated by other particle species.

3.3.1 Relevance of the time-dependent source term

The box model ACPIM, which was developed at the University of Manchester (Connolly et al., 2009), was used to calculate the ice formation within an ascending air parcel, using a prescribed ice nucleation parameterization. The ice nucleation parameterizations as described by Eqs. (16), (19) and (21) were analyzed for different updraft velocities and aerosol parameters as described in Table 2. Each parcel run is initialized at cirrus cloud conditions with $T = 235$ K, $p = 550$ mbar and RH$_{water} = 68\,\%$. The parcel is then allowed to develop for $t = 600$ s or for $t = 1200$ s at the lowest updraft velocity.

Figure 9 shows the decrease in temperature (Fig. 9a), the development of relative humidity over ice (Fig. 9b), and the

change in the temperature- and saturation-dependent function x_{therm} as defined in Eq. (13) (Fig. 9c). The ice fractions predicted by Eq. (16) (without time dependence) for different updraft velocities are depicted as a function of time (Fig. 9d) and in relation to the function xtherm (Fig. 9f) and in relation to temperature (Fig. 9e). For each updraft velocity value the trajectories were calculated for all aerosol parameters as described in Table 2.

- For the lowest updraft velocity ($w_1 = 0.05\,\mathrm{m\,s^{-1}}$), the reduction in temperature is less than 1 K over the whole simulated time period. Likewise, the increase in relative humidity over ice is less than 5 %. Thus, only a small supersaturation is reached. The temperature- and saturation-dependent function x_{therm} increases from $x_{therm} = 37$ to $x_{therm} = 42$. After $\Delta t = 1200\,\mathrm{s}$, the observed ice fractions remain below 2 %.

- For intermediate updraft velocities ($w_2 = 0.5\,\mathrm{m\,s^{-1}}$), the parcels are cooled to 232 K and reach peak relative humidity values of $RH_{ice} = 110\,\%$ at high aerosol concentrations and $RH_{ice} = 120\,\%$ at low aerosol concentrations. The increase in x_{therm} is strongly driven by the increase in relative humidity, and thus x_{therm} can reach peak values of $x_{therm} = 50$ and $x_{therm} = 65$. The observed ice fractions are strongly influenced by the aerosol concentrations and vary between 2 and 70 %.

- At very large updraft velocities ($w_3 = 5.0\,\mathrm{m\,s^{-1}}$), temperatures as low as 206 K are reached within 600 s. However, the determining factor for these simulations is the peak relative humidity, which is related to the prescribed aerosol concentration. At low aerosol concentrations, all aerosol particles are activated within less than 100 s. After the ice activation process is completed, the relative humidity value increases further to values larger than $RH_{ice} = 200\,\%$. For high aerosol concentrations, the conversion of all aerosol particles into ice crystals is only achieved at the end of the parcel run since the peak relative humidity ($RH_{ice} = 120\,\%$) is already reached within the first 100 s of the simulation while ice formation slows down after having reached peak relative humidity.

The graphs in Fig. 9g–j show simulations similar to those depicted in Fig. 9d, e and f. However, for the simulations presented in Fig. 9g–j the ice nucleation process was assumed to be time dependent according to Eqs. (19) and (21). Note that the temperature and relative humidity trajectories are very similar to the runs without time-dependent ice nucleation (Fig. 9a and b). Likewise, the evolution of x_{therm} is also similar.

When comparing the predicted ice fractions at the end of the updraft periods, the first time-dependent ice nucleation parameterization (Eq. 19) does not produce results deviating much from those based on Eq. (16). Only the initial increase of the observed ice fractions is steeper than for purely humidity- and temperature-dependent ice formation. The second time-dependent ice nucleation parameterization (Eq. 21) generally predicts ice-active fractions being higher than the purely x_{therm}-dependent parameterization by a factor of 2, which is largely due to the coefficient b_1 in Eq. (21). Note that the time-dependent ice nucleation parameterization described by Eq. (21) predicts rapid ice nucleation at low ice-active particle fractions. The measurements shown in Fig. 5 at least partially corroborate this result.

From this simple case study it can be concluded that the effect of time dependence is generally small and may only be relevant at low to moderate updraft velocities and for small ice-active particle fractions.

4 Conclusions and discussion

Deposition nucleation on ATD particles was investigated with AIDA cloud chamber experiments, following expansion trajectories starting from ice-subsaturated conditions at about 250, 235 or 223 K. The aerosol surface area concentrations and cooling rates were varied for all expansion experiments, because one of the goals of this experimental study was to determine the relevance of timescales to the observed ice nucleation efficiencies.

The ice nucleation efficiency observed for each experimental run was quantified by the measured ice nucleation thresholds at $f_{ice} = 1\,\%$, by deriving the INAS densities and by fitting the contact angle distribution parameters using nucleation rate formulations.

Ice nucleation onsets ($f_{ice} = 1\,\%$) were observed at relative humidities over ice between 118 and 121 % at warmer temperatures ($T_{start} \approx 250\,\mathrm{K}$), whereas ice activation of 1 % of all ATD particles occurred between 101 and 107 % at colder temperatures (T_{start} below 235 K). No direct relation between ice nucleation thresholds and cooling rates could be deduced from the experimental data. The time dependence of deposition nucleation was presumably small and could not be quantified from the ice nucleation thresholds. It should be noted that the observed freezing thresholds could also be partly explained by a freezing mechanism other than deposition nucleation, namely pore condensation freezing. Pore condensation freezing was proposed by Marcolli et al. (2014) as an explanation for freezing below water saturation. Note, however, that in our experimental setup we cannot clearly distinguish between these freezing mechanisms and thus make the assumption that ice nucleation is mostly caused by deposition nucleation.

INAS densities were derived for all experiments and were found to depend both on temperature T and the ice saturation ratio S_{ice} with

$$n_s(x_{therm}) = 1.88 \times 10^5 \cdot \exp(0.2659 \cdot x_{therm})\ [\mathrm{m^{-2}}], \quad (23)$$

where the temperature- and saturation-dependent function x_{therm} is defined by

$$x_{\text{therm}} = -(T - 273.2) + (S_{\text{ice}} - 1) \times 100. \qquad (24)$$

The INAS density approach was found to be independent of shifts in the particle size distribution, i.e., from shifting the median diameter from $d_{\text{med}} \approx 0.23\,\mu\text{m}$ to $d_{\text{med}} \approx 0.35\,\mu\text{m}$. As a parameterization for numerical models, the INAS density relation is only strictly valid for temperatures between 226 and 250 K and for humidities with $1 < S_{\text{ice}} < 1.2$. Especially at temperatures below 220 K, x_{therm} may be better described by a relation different from Eq. (24). Note that an extrapolation to lower temperatures relying on Eq. (24) would also predict very high INAS densities already at S_{ice} close to 1. To describe deposition nucleation even more precisely, x_{therm} could be parameterized as a higher-order function of temperature and relative humidity over ice in order to achieve a better match with observations, both at low temperatures above ice saturation and at higher temperatures close to water saturation. Deposition nucleation at higher temperatures should be investigated for a wider range of thermodynamic conditions in order to better characterize the dependence of x_{therm} on temperature and relative humidity and also for natural mineral dusts which are typically less ice-active than ATD particles (Möhler et al., 2006). Ice crystal concentrations predicted by $n_s(x_{\text{therm}})$ match the observed ice crystal concentrations for most experiments of this study within 1 order of magnitude regardless of the cooling rate or the aerosol surface area concentration.

In comparison to INAS density values derived from other empirical parameterizations or laboratory studies, the ice nucleation efficiency of ATD in deposition nucleation mode as derived from AIDA cloud chamber measurements is larger by at least 1 order of magnitude. Note that, in contrast to the parameterization derived from our measurements, the parameterizations by Phillips et al. (2012) and Meyers et al. (1992) suggest a much weaker or no temperature dependence of deposition nucleation.

Applying classical nucleation theory to the observed ice fractions yields average contact angle distribution parameters. For high-temperature deposition nucleation ($T_{\text{start}} \approx 250\,\text{K}$) the contact angle distribution parameters which best described all experimental runs ($r^2 = 0.48$) were $\mu_\theta = 22.1°$ and $\sigma_\theta = 0.095$. For deposition nucleation at lower temperatures, the contact angle parameters were found to be $\mu_\theta = 36.2°$ and $\sigma_\theta = 0.520$ ($r^2 = 0.52$) for experiments at $T_{\text{start}} \approx 235\,\text{K}$, and $\mu_\theta = 16.9°$ and $\sigma_\theta = 0.540$ ($r^2 = 0.89$) for $T_{\text{start}} \approx 220\,\text{K}$. The large variability of the contact angle distribution parameters suggests that the application of classical nucleation theory to deposition nucleation by certain aerosol species such as mineral dust would require a detailed investigation of the contact angle distribution parameters for different thermodynamic conditions. Additionally, the contribution of pore condensation freezing to heterogeneous nu-

cleation observed close to water saturation might lead to difficulties with applying classical nucleation theory directly.

The time dependence of deposition nucleation initiated by ATD particles was investigated by assuming that time dependence might be represented by either a linear source term $a_3 \cdot t$ or a factor describing the delayed activation of ice nucleation active surface sites according to $1 - \exp(-b_3 \cdot t)$. Note that, for $t \to \infty$, n_s is limited by two factors: first, the activation of all aerosol particles and, secondly, by the size of an active site which is assumed to cover $A_{\text{site}} = 10\,\text{nm}^2$ (Marcolli et al., 2007), with the surface area covered by active sites not exceeding the available aerosol surface area.

To evaluate the potential role of time-dependent ice nucleation in the atmosphere, the box model ACPIM was used to simulate the ascent of air parcels. For these case studies, ice nucleation was described by a purely thermodynamically driven INAS density function and two parameterizations with additional time-dependent terms. The time-dependent terms are potentially important at low to moderate updraft velocities and for small ice fractions. However, the results obtained from the three different parameterizations did not differ much from each other under the prescribed experimental conditions. It should be noted, however, that the modeling case studies in this work are based on ice nucleation results for ATD obtained under certain thermodynamic conditions.

The ATD experiments and modeling studies presented in this work are supposed to be a first step in rigorously investigating deposition nucleation over a wide temperature and saturation range in order to gain a better understanding of the factors which are relevant for deposition nucleation. This knowledge was then used to develop a metric which can be easily employed for the comparative analysis of other heterogeneous nucleation studies. Further investigations of atmospherically relevant dust samples are needed in order to better inform future parameterizations describing deposition ice nucleation.

Edited by: D. Knopf

References

Broadley, S. L., Murray, B. J., Herbert, R. J., Atkinson, J. D., Dobbie, S., Malkin, T. L., Condliffe, E., and Neve, L.: Immersion mode heterogeneous ice nucleation by an illite rich powder representative of atmospheric mineral dust, Atmos. Chem. Phys., 12, 287–307, doi:10.5194/acp-12-287-2012, 2012.

Chen, J.-P., Hazra, A., and Levin, Z.: Parameterizing ice nucleation rates using contact angle and activation energy derived from laboratory data, Atmos. Chem. Phys., 8, 7431–7449, doi:10.5194/acp-8-7431-2008, 2008.

Connolly, P. J., Möhler, O., Field, P. R., Saathoff, H., Burgess, R., Choularton, T., and Gallagher, M.: Studies of heterogeneous freezing by three different desert dust samples, Atmos. Chem. Phys., 9, 2805–2824, doi:10.5194/acp-9-2805-2009, 2009.

Eastwood, M. L., Cremel, S., Wheeler, M., Murray, B. J., Girard, E., and Bertram, A. K.: Effects of sulfuric acid and ammonium sulfate coatings on the ice nucleation properties of kaolinite particles, Geophys. Res. Lett., 36, L02811, doi:10.1029/2008GL035997, 2009.

Fahey, D. W., Gao, R.-S., Möhler, O., Saathoff, H., Schiller, C., Ebert, V., Krämer, M., Peter, T., Amarouche, N., Avallone, L. M., Bauer, R., Bozóki, Z., Christensen, L. E., Davis, S. M., Durry, G., Dyroff, C., Herman, R. L., Hunsmann, S., Khaykin, S. M., Mackrodt, P., Meyer, J., Smith, J. B., Spelten, N., Troy, R. F., Vömel, H., Wagner, S., and Wienhold, F. G.: The AquaVIT-1 intercomparison of atmospheric water vapor measurement techniques, Atmos. Meas. Tech. Discuss., 7, 3159–3251, doi:10.5194/amtd-7-3159-2014, 2014.

Fletcher, N. H.: Active sites and ice crystal nucleation, J. Atmos. Sci., 26, 1266–1271, doi:10.1175/1520-0469(1969)026<1266:ASAICN>2.0.CO;2, 1969.

Hiranuma, N. and Paukert, M. and Steinke, I. and Zhang, K. and Kulkarni, G. and Hoose, C. and Schnaiter, M. and Saathoff, H. and Möhler, O.: A comprehensive parameterization of heterogeneous ice nucleation of dust surrogate: laboratory study with hematite particles and its application to atmospheric models, Atmos. Chem. Phys., 23, 13145–13158, doi:acp-14-13145-2014,2014.

Hoose, C. and Möhler, O.: Heterogeneous ice nucleation on atmospheric aerosols: a review of results from laboratory experiments, Atmos. Chem. Phys., 12, 9817–9854, doi:10.5194/acp-12-9817-2012, 2012.

Koehler, K. A., Kreidenweis, S. M., DeMott, P. J., Petters, M. D., Prenni, A. J., and Möhler, O.: Laboratory investigations of the impact of mineral dust aerosol on cold cloud formation, Atmos. Chem. Phys., 10, 11955–11968, doi:10.5194/acp-10-11955-2010, 2010.

Lüönd, F., Stetzer, O., Welti, A., and Lohmann, U.: Experimental study on the ice nucleation ability of size-selected kaolinite particles in the immersion mode, J. Geophys. Res., 115, D14201, doi:10.1029/2009JD012959, 2010.

Marcolli, C., Gedamke, S., Peter, T., and Zobrist, B.: Efficiency of immersion mode ice nucleation on surrogates of mineral dust, Atmos. Chem. Phys., 7, 5081–5091, doi:10.5194/acp-7-5081-2007, 2007.

Marcolli, C.: Deposition nucleation viewed as homogeneous or immersion freezing in pores and cavities, Atmos. Chem. Phys., 4, 2071–2104, doi:10.5194/acp-14-2071-2014, 2014.

Meyers, M. P., DeMott, P. J., and Cotton, W. R.: New primary ice-nucleation parameterizations in an explicit cloud model, J. Appl. Meteorol., 31, 708–721, doi:10.1175/1520-0450(1992)031<0708:NPINPI>2.0.CO;2, 1992.

Möhler, O., Field, P. R., Connolly, P., Benz, S., Saathoff, H., Schnaiter, M., Wagner, R., Cotton, R., Krämer, M., Mangold, A., and Heymsfield, A. J.: Efficiency of the deposition mode ice nucleation on mineral dust particles, Atmos. Chem. Phys., 6, 3007–3021, doi:10.5194/acp-6-3007-2006, 2006.

Möhler, O., Benz, S., Saathoff, H., Schnaiter, M., Wagner, R., Schneider, J., Walter, S., Ebert, V., and Wagner, S.: The effect of organic coating on the heterogeneous ice nucleation efficiency of mineral dust aerosols, Environ. Res. Lett., 3, 025007, doi:10.1088/1748-9326/3/2/025007, 2008.

Murphy, D. M. and Koop, T.: Review of the vapour pressures of ice and supercooled water for atmospheric applications, Q. J. Roy. Meteor. Soc., 131, 1539–1565, doi:10.1256/qj.04.94, 2005.

Murray, B. J., Broadley, S. L., Wilson, T. W., Atkinson, J. D., and Wills, R. H.: Heterogeneous freezing of water droplets containing kaolinite particles, Atmos. Chem. Phys., 11, 4191–4207, doi:10.5194/acp-11-4191-2011, 2011.

Murray, B. J., O'Sullivan, D., Atkinson, J. D., and Webb, M. E.: Ice nucleation by particles immersed in supercooled cloud droplets, Chem. Soc. Rev., 41, 6519–6554, doi:10.1039/c2cs35200a, 2012.

Niedermeier, D., Shaw, R. A., Hartmann, S., Wex, H., Clauss, T., Voigtländer, J., and Stratmann, F.: Heterogeneous ice nucleation: exploring the transition from stochastic to singular freezing behavior, Atmos. Chem. Phys., 11, 8767–8775, doi:10.5194/acp-11-8767-2011, 2011.

Niemand, M., Möhler, M., Vogel, B., Vogel, H., Hoose, C., Connolly, P., Klein, H., Bingemer, H., DeMott, P., Skrotzki, J., and Leisner, T.: A particle-surface-area based parameterization of immersion freezing on desert dust particles, J. Atmos. Sci., 69, 3077–3092, doi:10.1175/JAS-D-11-0249.1, 2012.

Phillips, V. T. J., DeMott, P. J., and Andronache, C.: An empirical parameterization of heterogeneous ice nucleation for multiple chemical species of aerosol, J. Atmos. Sci., 65, 2757–2783, doi:10.1175/2007JAS2546.1, 2008.

Phillips, V. T. J., DeMott, P. J., Andronache, C., Pratt, K. A., Prather, K. A., Subramanian, R., and Twohy, C.: Improvements to an empirical parameterization of heterogeneous ice nucleation and its comparison with observations, J. Atmos. Sci., 70, 378–409, doi:10.1175/JAS-D-12-080.1, 2012.

Pruppacher, H. R. and Klett, J. D.: Microphysics of Clouds and Precipitation, Atmospheric and Oceanographic Sciences Library, 2nd rev., and enl. edn., 18, Kluwer, Dordrecht, 1997.

Rigg, Y. J., Alpert, P. A., and Knopf, D. A.: Immersion freezing of water and aqueous ammonium sulfate droplets initiated by humic-like substances as a function of water activity, Atmos. Chem. Phys., 13, 6603–6622, doi:10.5194/acp-13-6603-2013, 2013.

Schnaiter, M., Büttner, S., Möhler, O., Skrotzki, J., Vragel, M., and Wagner, R.: Influence of particle size and shape on the backscattering linear depolarisation ratio of small ice crystals – cloud chamber measurements in the context of contrail and cirrus microphysics, Atmos. Chem. Phys., 12, 10465–10484, doi:10.5194/acp-12-10465-2012, 2012.

Sullivan, R. C., Miñambres, L., DeMott, P. J., Prenni, A. J., Carrico, C. M., Levin, E. J. T., and Kreidenweis, S. M.: Chemical processing does not always impair heterogeneous ice nucleation of mineral dust particles, Geophys. Res. Lett., 37, L24805, doi:10.1029/2010GL045540, 2010.

Vali, G.: Nucleation terminology, J. Aerosol Sci., 16, 575–576, 1985.

Vali, G.: Freezing rate due to heterogeneous nucleation, J. Atmos. Sci., 51, 1843–1856, doi:10.1175/1520-0469(1994)051<1843:FRDTHN>2.0.CO;2, 1994.

Vali, G.: Repeatability and randomness in heterogeneous freezing nucleation, Atmos. Chem. Phys., 8, 5017–5031, doi:10.5194/acp-8-5017-2008, 2008.

Vlasenko, A., Sjögren, S., Weingartner, E., Gäggeler, H. W., and Ammann, M.: Generation of submicron Arizona test dust aerosol: chemical and hygroscopic properties, Aerosol Sci. Tech., 39, 452–460, doi:10.1080/027868290959870, 2005.

Wagner, R., Linke, C., Naumann, K.-H., Schnaiter, M., Vragel, M., Gangl, M., and Horvath, H.: A review of optical measurements at the aerosol and cloud chamber AIDA, J. Quant. Spectrosc. Ra., 110, 930–949, doi:10.1016/j.jqsrt.2009.01.026, 2009.

Welti, A., Lüönd, F., Stetzer, O., and Lohmann, U.: Influence of particle size on the ice nucleating ability of mineral dusts, Atmos. Chem. Phys., 9, 6705–6715, doi:10.5194/acp-9-6705-2009, 2009.

Westbrook, C. D.: The fall speeds of sub-100 μm ice crystals, Q. J. Roy. Meteor. Soc., 134, 1243–1251, doi:10.1002/qj.290, 2008.

Wheeler, M. J. and Bertram, A. K.: Deposition nucleation on mineral dust particles: a case against classical nucleation theory with the assumption of a single contact angle, Atmos. Chem. Phys., 12, 1189–1201, doi:10.5194/acp-12-1189-2012, 2012.

Yakobi-Hancock, J. D., Ladino, L. A., and Abbatt, J. P. D.: Feldspar minerals as efficient deposition ice nuclei, Atmos. Chem. Phys., 13, 11175–11185, doi:10.5194/acp-13-11175-2013, 2013.